

UC San Diego

UC San Diego Previously Published Works

Title

The mechanics and dynamics of cancer cells sensing noisy 3D contact guidance.

Permalink

<https://escholarship.org/uc/item/8hs1n0tx>

Journal

Proceedings of the National Academy of Sciences, 118(10)

Authors

Kim, Jihan

Cao, Yuansheng

Eddy, Christopher

et al.

Publication Date

2021-03-09

DOI

10.1073/pnas.2024780118

Peer reviewed

The mechanics and dynamics of cancer cells sensing noisy 3D contact guidance

Jihan Kim^{a,1}, Yuansheng Cao^{b,1} , Christopher Eddy^a, Youyuan Deng^c , Herbert Levine^{c,d,e,2} , Wouter-Jan Rappel^{b,2} , and Bo Sun^{a,2} 

^aDepartment of Physics, Oregon State University, Corvallis, OR 97331; ^bDepartment of Physics, University of California San Diego, La Jolla, CA 92093; ^cCenter for Theoretical Biological Physics, Northeastern University, Boston, MA 02115; ^dDepartment of Physics, Northeastern University, Boston, MA 02115; and ^eDepartment of Bioengineering, Northeastern University, Boston, MA 02115

Contributed by Herbert Levine, January 20, 2021 (sent for review December 1, 2020; reviewed by Guillaume Duclos and Ming Guo)

Contact guidance is a major physical cue that modulates cancer cell morphology and motility, and is directly linked to the prognosis of cancer patients. Under physiological conditions, particularly in the three-dimensional (3D) extracellular matrix (ECM), the disordered assembly of fibers presents a complex directional bias to the cells. It is unclear how cancer cells respond to these noncoherent contact guidance cues. Here we combine quantitative experiments, theoretical analysis, and computational modeling to study the morphological and migrational responses of breast cancer cells to 3D collagen ECM with varying degrees of fiber alignment. We quantify the strength of contact guidance using directional coherence of ECM fibers, and find that stronger contact guidance causes cells to polarize more strongly along the principal direction of the fibers. Interestingly, sensitivity to contact guidance is positively correlated with cell aspect ratio, with elongated cells responding more strongly to ECM alignment than rounded cells. Both experiments and simulations show that cell–ECM adhesions and actomyosin contractility modulate cell responses to contact guidance by inducing a population shift between rounded and elongated cells. We also find that cells rapidly change their morphology when navigating the ECM, and that ECM fiber coherence modulates cell transition rates between different morphological phenotypes. Taken together, we find that subcellular processes that integrate conflicting mechanical cues determine cell morphology, which predicts the polarization and migration dynamics of cancer cells in 3D ECM.

contact guidance | extracellular matrix | cell motility | phenotypic transition

Cell polarization and directed migration are critical in morphogenesis, wound healing, and cancer metastasis (1–4). During these processes, upstream chemical and mechanical sensory apparatus are coupled to cytoskeleton regulators, leading to downstream morphological and motility responses (5, 6). Under physiological conditions, cells have to integrate multiple guidance cues that are often noisy or conflicting (7). This is particularly the case for cells that navigate in three-dimensional (3D) tissue space where the extracellular matrix (ECM) fibers present, through a process known as contact guidance, a disordered set of directional cues to the cell (8). Understanding the mechanisms, robustness, and limitations of cell responses to non-perfect contact guidance signals is pivotal in our quest to predict and engineer cell behaviors (9–11).

Contact guidance by fibers represents a major mechanical mechanism that significantly biases cell polarization and migration (12, 13). On 2D substrates, fabricated topographical features such as parallel arrays of grooves bias focal adhesion formation and actin polymerization (14–18). As a result, adherent cells tend to elongate and align their major axes as well as velocity to the topographical features. Contact guidance has also been observed for cells in 3D ECMs. For instance, we and other groups have shown that ECM fiber alignment, either engineered by external stress or induced by cell-generated forces, is able to bias the polarization and migration of cancer cells in vitro (19, 20). Clinically,

contact guidance regulates metastasis of cancer cells during dissemination and thus correlates with the prognosis of cancer patients (21).

While much has been learned about contact guidance for cells on 2D substrates, 3D contact guidance differs in both biological and physical aspects and remains poorly understood. Biologically, 3D cell mechanosensing and migration programs are distinct from their 2D counterparts (22, 23). As a result, cell morphology, morphodynamics, and migration characteristics significantly depend on the dimensionality of the environment (24–26). Physically, 3D ECM consists of a disordered network in which cross-linked or physically entangled ECM fibers display a wide range of angles (27). As a result, cells in 3D ECM constantly experience noisy, incoherent contact guidance cues.

In order to understand how cells respond to incoherent contact guidance cues, we combine experiments, theoretical modeling, and computer simulations. In particular, we study invasive breast cancer cells in type I collagen ECM in which we can quantitatively control the level of ECM alignment. We find that there exist subgroups of cells, differing in morphology, that exhibit distinct sensitivity to contact guidance cues. Our experiments show that both cell–ECM adhesions and actomyosin contractility modulate cell responses to contact guidance by inducing a population shift among these subgroups. These results are consistent with a computational model in which the cell morphology is determined by a balance between cell–fiber adhesion forces

Significance

The spatial organization of ECM fibers biases the polarization and migration of cancer cells, a phenomenon known as contact guidance which is directly linked to the clinical outcome of cancers. In physiological conditions, ECM fibers do not align perfectly in parallel. Therefore, we study the morphological and migrational response of breast cancer cells to ECM fibers aligned to various degrees. We identify the cell's aspect ratio as an integrated biomarker that determines its sensitivity to contact guidance cues. We also find that the level of ECM alignment modulates transitions between cells of differing morphology. Taken together, we show that cells integrate complex mechanical cues to determine their morphodynamics, thereby controlling polarization and migration in 3D ECM.

Author contributions: H.L., W.-J.R., and B.S. designed research; J.K., Y.C., C.E., Y.D., W.-J.R., and B.S. performed research; J.K., Y.C., C.E., H.L., W.-J.R., and B.S. analyzed data; and H.L., W.-J.R., and B.S. wrote the paper.

Reviewers: G.D., Brandeis University; and M.G., Massachusetts Institute of Technology.

The authors declare no competing interest.

Published under the [PNAS license](#).

¹J.K. and Y.C. contributed equally to this work.

²To whom correspondence may be addressed. Email: h.levine@northeastern.edu, rappel@physics.ucsd.edu, or sunb@onid.orst.edu.

This article contains supporting information online at <https://www.pnas.org/lookup/suppl/doi:10.1073/pnas.2024780118/-/DCSupplemental>.

Published March 3, 2021.

and contractile forces. We also find that cells rapidly adjust their morphology when navigating the ECM, and that the level of ECM fiber alignment modulates cell transition rates between different morphological phenotypes. Our results indicate that subcellular processes that integrate conflicting mechanical cues determine cell morphology, and that this morphology then determines the polarization and migration dynamics of cancer cells in 3D ECM.

Results

In order to control the level of ECM fiber alignment, we utilize magnetofluidics techniques to align fibers during the gelation process of a type I collagen matrix. In our experimental setup, an iron particle of approximately 150- μm radius is rotated by a strong magnetic field (Fig. 1A). When embedded in neutralized collagen solution, the resulting vortex flow aligns collagen fibers (28). As the flow speed decreases in the radial direction away from the particle, the level of collagen fiber alignment also decreases. As a result, cells cultured inside the collagen ECM experience spatially dependent contact guidance cues.

To assess the level of ECM alignment, we image the collagen fibers using confocal reflection microscopy (Fig. 1B), and quantify the fiber images within windows of size $100\ \mu\text{m} \times 100\ \mu\text{m}$. Because ECM fibers do not have distinguishable front and back ends, the alignment of the fibers can be described by the

nematic order (29, 30). Using image analysis (31), we determine the principal fiber axis that characterizes the direction of contact guidance, as well as the structural coherence c , which measures the strength of contact guidance (Fig. 1C). This coherence ranges from $c = 1$, corresponding to all fibers aligned perfectly along the principal axis, to $c = 0$, corresponding to fibers that are aligned randomly (SI Appendix, section S1). As expected from the flow field, we find that the coherence decreases as a function of the radial distance ρ (Fig. 1D). In addition, and consistent with previous reports (32, 33), spatial fluctuations of nematic order are observed, due to the disordered nature of the collagen ECM. Since cells sense the local ECM structure rather than bulk ECM properties, we focus on contact guidance cues measured in the vicinity of single cells (34).

We first quantify how cell morphology responds to 3D contact cues with varying levels of coherence. To this end, we culture MDA-MB-231 breast cancer cells in the devices where collagen ECM is aligned via vortex flows. To avoid significant cell–cell interactions, we choose a cell density of less than $200/\mu\text{L}$ in all experiments. Within each image subwindow of $100 \times 100\ \mu\text{m}^2$ where a cell is centered, we measure the ECM nematic order as characterized by its principal direction and coherence c . We also measure the cell morphological properties as characterized by the cell's major axis direction and aspect ratio a using its minimally enclosing ellipse.

Fig. 2A shows a typical image subwindow containing a single cell. We define the deviation angle $\delta\theta$ as the acute angle between the cell's major axis (pink line) and ECM principal axis (yellow line). The latter axis is determined by representing the local geometry of collagen ECM as an orientation ellipse (yellow ellipse), whose eccentricity equals the coherence c and whose major axis points to the principal direction of collagen fibers. Comparing the cell orientation and the ECM principal axis for 550 cells, we find that the deviation angle is not only controlled by the ECM coherence but also critically depends on the cell aspect ratio (Fig. 2B; see also SI Appendix, Fig. S1). For almost rounded cells with small aspect ratios, the cosine of the deviation angle distributes broadly between zero and one, indicating that the deviation angle is essentially random. In contrast, elongated cells with large aspect ratios exhibit small deviation angles, and thus values of the cosine close to one. Furthermore, these cells are much more likely to be observed in regions of the ECM with higher coherence (Fig. 2B; see also SI Appendix, Fig. S1).

To better illustrate how cell polarization is jointly regulated by the strength of contact guidance and cell morphology, we empirically categorize the cells based on their aspect ratios a as either rounded ($a < 2$), elongated ($a > 3$), or intermediate ($2 < a < 3$) subgroups following previous conventions (35). For each subgroup, we calculate the fraction of cells that are well-aligned with the ECM—defined here as having a deviation angle less than 20° —as a function of the fiber coherence (Fig. 2C). We find that, for both intermediate and elongated shapes, the fraction of well-aligned cells rapidly increases with ECM coherence c , indicating that stronger contact guidance cues can more effectively steer cells. In contrast, the fraction of rounded cells that are aligned shows little dependence on the coherence, illustrating that these cells largely ignore cues from the ECM alignment.

The observations in Fig. 2C suggest that the aspect ratio may be a critical factor in determining the sensitivity of a cell to contact guidance. The coherence of ECM alignment—a nematic order parameter—modulates cell shape and aspect ratio, which, in turn, control the cell polarization with respect to the principal direction. Indeed, we find that higher coherence shifts the distribution of cell shapes toward greater aspect ratios (Fig. 2D), therefore causing more cells to polarize in the direction of contact guidance.

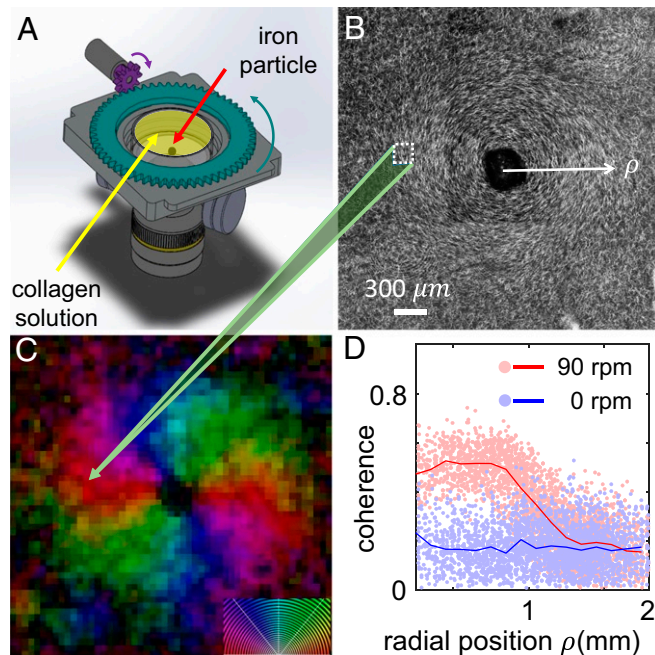


Fig. 1. Experimental setup that controls the level of ECM alignment for 3D cell cultures. (A) Schematics of our device. A magnetic field is applied to rotate an iron particle and creates a vortex flow during the gelation process of type I collagen solution. Rotation speed is controlled by a motorized stage. (B) Confocal reflection image shows that, at a rate of 90 rpm, the vortex flow causes an alignment of collagen fibers that critically depends on the radial position ρ from the center of the iron particle. (C) The geometric characterization of the collagen ECM represented in the HSV color space. Here the H (hue) channel represents the direction of collagen fibers (see *Inset* for the color legend), V channel (value, varies from zero to one, or dark to bright) is directly mapped to coherence, and S channel is fixed at one. (D) Local coherence as a function of radial position for rotation speeds of 90 rpm (red) and 0 rpm (blue). Dots, results from individual sampling windows of $100 \times 100\ \mu\text{m}^2$; lines, a sliding average with window size of $50\ \mu\text{m}$ in the ρ dimension.

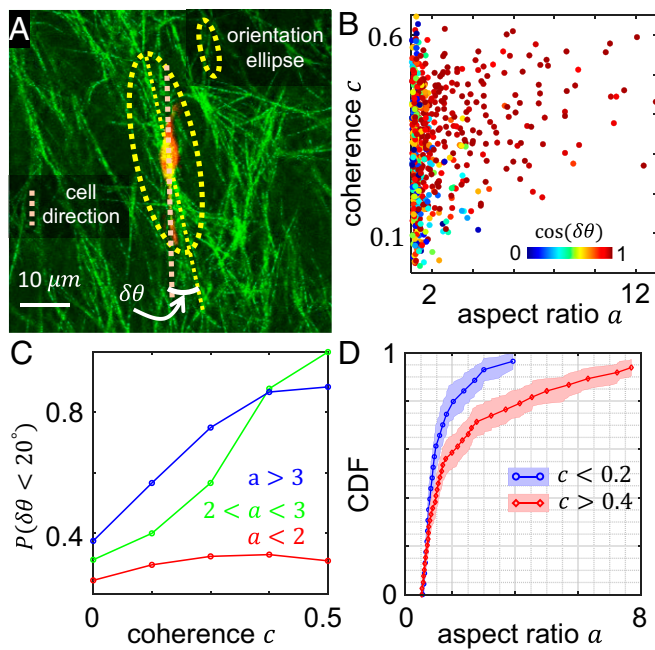


Fig. 2. Cell morphology and local ECM geometry synergistically determine the orientation of cells. (A) Subwindow containing a cell (red) and collagen fibers (green). Also shown are the deviation angle $\delta\theta$ between the long axis (pink line) of the cell and the principal direction (yellow line) of the local collagen fibers, determined using the orientation ellipse of the local ECM (yellow ellipse). (B) Scatter plot of cell aspect ratio a with respect to their local ECM coherence c . Colors of the dots represent $\cos(\delta\theta)$, where $\delta\theta$ is the deviation angle. (C) The fraction of well-aligned cells ($\delta\theta < 20^\circ$) at varying local ECM coherence c . The cells are divided into three subgroups based on their aspect ratios a : red, $a < 2$; green, $2 < a < 3$; and blue, $a > 3$. Along the horizontal axis, data are binned by coherence, with a bin size of 0.1. For $a < 2$, $P < 0.4$ Cochran–Armitage test for trend. For $2 < a < 3$ and $a > 3$, $P < 0.05$ Cochran–Armitage test for trend. (D) Cumulative distribution function (CDF) of the cell aspect ratio for cells in weakly aligned ECM (blue circles, $c < 0.2$), and in highly aligned ECM (red diamonds, $c > 0.4$). Shaded area show 95% CIs estimated using Greenwood’s formula. Data in B–D cover 550 cells from three independent experiments.

To gain insights into our experimental findings, we construct a 2D computational model that computes the morphology of a single cell on a collection of fibers with controllable degrees of coherence. Our model is formulated using the cellular Potts model (see *SI Appendix* for details). This model, originally formulated to describe cell sorting (36), can be used to model individual cells as well as tissue behavior (37–40). In the model, space is discretized using a regular square grid, and each grid site i, j is assigned a “spin” value $\sigma_{i,j}$. The cell is defined as a set of connected sites, which are assigned a “spin” value $\sigma_{i,j} = 1$, while sites not associated with the cell are assigned a spin value $\sigma_{i,j} = 0$. Cell morphodynamics is implemented via a Monte Carlo update of the spins that minimizes the Hamiltonian H given below. In our simulations, we select, at random, a site of the lattice and change its spin provisionally to one of its randomly selected nearest neighbors. To determine the probability of change, we compute the difference in energy, ΔH , before and after the change. For $\Delta H < 0$, we accept the change, and, for $\Delta H > 0$, we accept it with a probability $\exp(-\Delta H/T)$, where T is an effective temperature. We define one Monte Carlo step (MCS) to be a successful change of a single spin.

The Hamiltonian in our model is given by $H = \sum_{(i,j)\text{neighbors}} J_{cm}[1 - \delta(\sigma_i, \sigma_j)] + \lambda(A - A_0)^2 - \sum_{i,j} J_{cf}\zeta_{i,j}\sigma_{i,j}$. Here, the first term is a sum over all neighbors of sites i, j of the

lattice, and δ is the Kronecker delta. This term, parameterized by J_{cm} , describes the cell contractility together with the membrane tension. Both contractility and tension will reduce the contact area of the cell membrane and surrounding medium. Since $J_{cm} > 0$, an increase in the contact area will therefore increase the Hamiltonian, which is energetically unfavorable. The second term in the Hamiltonian is an energy penalty, with strength λ , for deviating from the prescribed cell area A_0 .

The fiber networks in our simulations are generated using a biased random walk method (see *SI Appendix*, section S2). In this method, each growth step of the fiber is drawn from a normal distribution $N(0, \Delta\phi)$, where $\Delta\phi$ is the standard deviation between each step. Thus, larger values of $\Delta\phi$ lead to less coherent fiber networks. The fiber density is chosen in such a way that the average number of the fibers that overlaps with the cell is comparable to experiments (projection from 3D to 2D). To allow for a direct comparison between simulations and experimental results, we compute the coherence of the resulting fiber networks using the same algorithm used to quantify the coherence of the experimental collagen matrices (see *SI Appendix*, section S2 and Fig. S2). The final term in the Hamiltonian takes into account the adhering interaction between the cell and the fibers, parameterized by J_{cf} . This term is only nonzero if the site contains both a fiber ($\zeta_{i,j} = 1$) and the cell ($\sigma_{i,j} = 1$). Notice that the term with J_{cf} is negative so that it is energetically favorable for the cell to adhere to a fiber. The ratio $\gamma = J_{cf}/J_{cm}$ measures the relative strength of cell adhesion compared to cell contractility. For example, elevated cell–fiber adhesion, modeled by taking larger values of J_{cf} , or treatment by blebbistatin, which reduces the myosin-based cell contractility and is modeled by reducing J_{cm} , both correspond to an increased γ in the model. For each network, we perform simulations on a 50×50 grid, using 10^6 MCSs, after which we determine the cell aspect ratio a and cell–fiber deviation angle $\delta\theta$ as in the experimental images (compare Fig. 2A). Parameter values used in the simulations are given in *SI Appendix*, Table S1.

Examples of two randomly generated networks and the resulting cell morphologies are shown in Fig. 3A for a network with a relatively large ($c = 0.7$, $\Delta\phi = 15^\circ$; Fig. 3A, Upper) and low coherence ($c = 0.1$, $\Delta\phi = 75^\circ$; Fig. 3A, Lower). Clearly, the highly coherent network exhibits fibers that are mostly aligned, while the network with low coherence has many fibers that cross at large angles. As a result of the fiber structure, the cell in the high coherent network is more aligned with the fibers and displays a larger aspect ratio than the one for the low coherent network ($a = 3.1$ vs. $a = 1.2$; quantified using fitting to an ellipse as described in *SI Appendix*).

To determine how fiber architecture and model parameters affect cell morphology and alignment, we generate a large number of networks with values of $\Delta\phi$ that result in a computed coherence that is in the range of the experiments ($c < 0.7$). Keeping all other parameters fixed, we systematically vary the ratio $\gamma = J_{cf}/J_{cm}$ within the range of [0,3]. The results of 10^4 simulations are shown in Fig. 3B, where each dot represents the outcome of a single simulation. For fiber networks with low coherence (large $\Delta\phi$), most cells are found to have aspect ratios close to one, corresponding to rounded shapes. Increasing the coherence, however, results in more and more cells with higher aspect ratio, corresponding to elongated cells.

To determine how the cell–fiber alignment depends on the aspect ratio, we divide, as in the experiments, the results of the simulations into three subgroups based on the aspect ratio of the cell ($a < 2$, or rounded; $2 < a < 3$, or intermediate; and $a > 3$, or elongated) and compute the fraction of cells that have a deviation angle less than 20° . The results are shown in Fig. 3C and reveal that the distribution of cell–fiber deviation angles is qualitatively similar to experimental observations (Fig. 2C). Specifically, the fraction of well-aligned cells is larger for cells

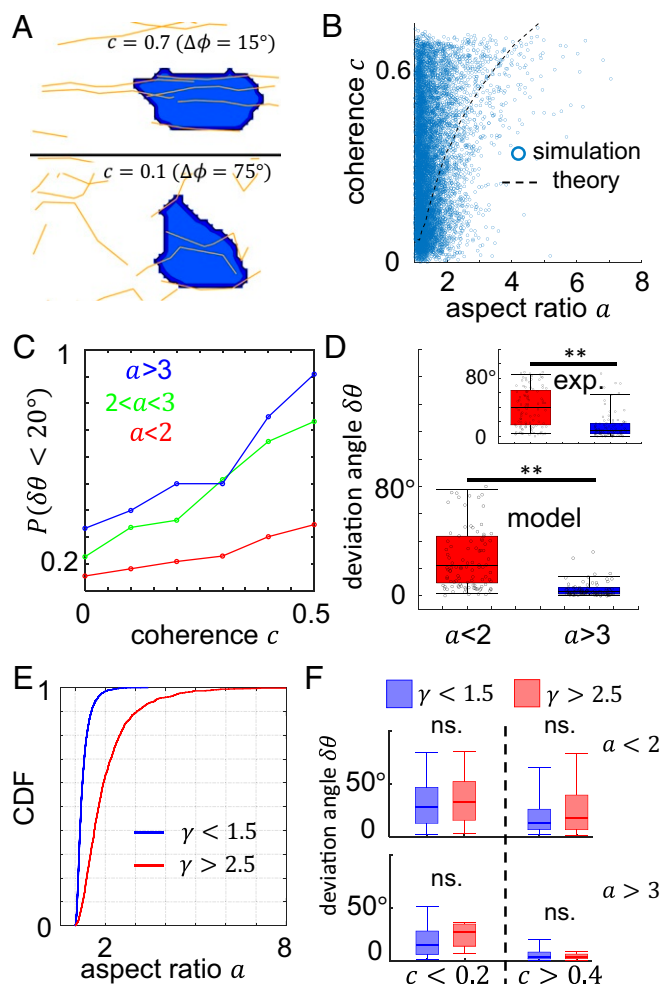


Fig. 3. Cellular Potts model of cell–fiber interactions. (A) Two examples of cell morphologies obtained using a cellular Potts model and fiber networks with high ($c = 0.7$, $\Delta\phi = 15^\circ$) and low ($c = 0.1$, $\Delta\phi = 75^\circ$) coherence. (B) Computed cell aspect ratio and fiber network coherence using 10,000 simulated networks. Dashed line corresponds to the analytical formula derived in *SI Appendix*, section S2. See also *SI Appendix*, Fig. S4 for a probability heat map of the simulated data points. (C) Fraction of well-aligned cells, defined as $\delta\theta < 20^\circ$, for varying coherence values c . Similar to Fig. 2C, the cells are divided into three subgroups based on their aspect ratios a : red, $a < 2$; green, $2 < a < 3$; and blue, $a > 3$. (D) Distribution of cell–fiber deviation angles for cells grouped using their aspect ratio. The main plot is the model result. *Inset* is experimental result. Red, cells with aspect ratio less than two; blue, cells with aspect ratio greater than three. $**P < 0.01$ with ANOVA test. (E) CDF of cell aspect ratio for two different values of $\gamma = J_{cf}/J_{cm}$. (F) Distribution of the deviation angles $\delta\theta$ for cells obtained in simulations with $\gamma < 1.5$ and with $\gamma > 2.5$ for networks with low (*Left*) and high (*Right*) coherence, and for cells with low ($a < 2$; *Upper*) and high ($a > 2$; *Lower*) values of the aspect ratio.

with higher aspect ratio and increases for increasing values of the coherence. When grouped as rounded and elongated shapes, cells in each group show significantly different distributions of deviation angles (Fig. 3D), which is consistent with experimental observations (Fig. 3D, *Inset*). The morphology-dependent cellular response to contact guidance is not unique to Potts model. In fact, a model we previously developed (41) also shows that deviation angle decreases with cell aspect ratio, and increases with the level of ECM alignment (*SI Appendix*, Fig. S5). Together, these simulation results support the experimental observations and highlight the critical role of cell morphology in regulating contact guidance directed cell polarization.

Our simulation results show that, in high-coherence networks, the cell is more likely to take on an elongated shape with its major axis aligned with the average fiber orientation. This finding can be explained by considering the special case of an ellipsoidal cell positioned on two cross-linked fibers (see *SI Appendix*, Fig. S3A). For this case, we can obtain an analytical formula for the aspect ratio of the cell as a function of the angle between the two fibers and the ratio of contraction/protrusion and cell–fiber adhesion. Specifically, we can show that the aspect ratio increases as the fiber angle decreases (*SI Appendix*, Fig. S3B). This formula can also be used to fit the simulation results in Fig. 3B (dashed line), which shows that, consistent with the experimental results, a more coherent fiber network will result in more aligned cells with larger aspect ratios.

To further elucidate the relationship between cell morphology, cell–fiber deviation angle, and model parameters, we compute the CDF of the aspect ratio for two different values of γ . We find that increasing γ , corresponding to a relative increase of the cell–fiber adhesion, leads to more elongated cells (Fig. 3E). Importantly, varying γ does not affect the sensitivity of cells to contact guidance (Fig. 3F). This is apparent if we examine cells within each morphological category (rounded, $a < 2$; or elongated, $a > 3$) or for different values of coherence. For all cases, cells with small and large γ have the same mean deviation angles with respect to the mean fiber orientation. Thus, our model predicts that the relative strength of the cell–fiber adhesion and cell contractility only indirectly affects the alignment through its change of aspect ratio.

Our simulation models predict that the sensitivity of a cell to contact guidance cues is primarily determined by its aspect ratio. To test this prediction, we experimentally vary the cell–ECM adhesion and cell contractility in an independent fashion. We first incorporate fibronectin proteins (FN) into the collagen matrix in order to enhance cell–ECM adhesion (12). Cell aspect ratio is higher in FN–collagen ECM, which is consistent with the cell morphology predicted by our model (Fig. 4A). To quantify the sensitivity of cells to contact guidance cues, we compare the deviation angles of cells in pure collagen and in FN–collagen ECM as shown in Fig. 4B. While higher coherence and larger aspect ratio are associated with smaller deviation angles, we find that increasing cell–ECM adhesion does not significantly affect the deviation angle, neither for rounded ($a < 2$) or elongated ($a > 3$) shapes and neither in weakly ($c < 0.2$) or strongly ($c > 0.4$) aligned ECM. Previous reports have suggested that increasing cell–ECM adhesion facilitates cell mechanosensing of contact guidance cues (12, 42). Here we show that the effect is linked to an increase in cell aspect ratio.

We next compare the deviation angles of cells after treatment with blebbistatin, which reduces myosin-associated contractility. Consistent with both our model prediction (Fig. 3E) and previous observations (12), blebbistatin-treated cells are more elongated (Fig. 4C). Similar to the effects of increasing cell–ECM adhesion, we find that the primary function of blebbistatin in modulating contact guidance is by shifting cell morphology. Once conditioned by cell aspect ratio a , and ECM coherence c , blebbistatin-treated and nontreated cells exhibit similar distributions of deviation angles (Fig. 4D).

After examining the morphological response of cells to contact guidance cues, we next study the cell motility response by time-lapse confocal imaging. We use a $4\times$ low-magnification lens to image the cells in order to obtain a larger field of view that spans areas with both small and large coherence. As shown by the temporal projection in Fig. 5A, cells in regions with strong contact guidance cues (near the central particle, small ρ) move preferably in the tangential direction. Cells in regions with weak contact guidance cues (far away from the central particle, large ρ), on the other hand, generally move more randomly.

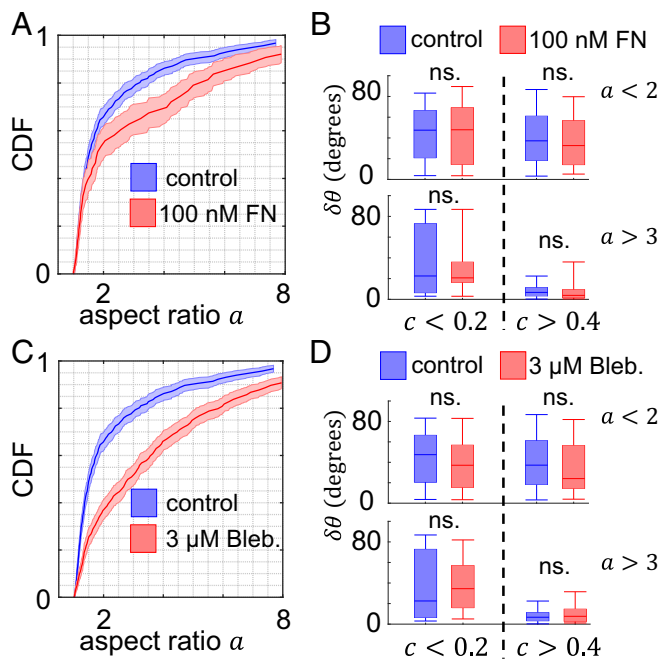


Fig. 4. Cell-ECM adhesion and intracellular force generation modulate cell responses to contact guidance. (A) The CDF of the aspect ratio for cells in ECM consisting of collagen and fibronectin (red) and of only collagen (blue). Shaded areas show 95% CIs estimated using Greenwood's formula. For FN, ECM consists of 1.5 mg/mL collagen and additional fibronectin; for control, ECM consists of 1.5 mg/mL collagen. (B) Deviation angles analyzed for rounded ($a < 2$) and elongated ($a > 3$) cells, in ECM regions that are weakly aligned ($c < 0.2$) and highly aligned ($c > 0.4$). Statistical comparisons are carried out using ANOVA; ns., not significant. (C) CDF of cell aspect ratio of blebbistatin-treated cells (red) and untreated cells (blue). Shaded area show 95% CIs estimated using Greenwood's formula. (D) Deviation angles analyzed for rounded ($a < 2$) and elongated ($a > 3$) cells, in ECM regions that are weakly aligned ($c < 0.2$) and highly aligned ($c > 0.4$). Statistical comparisons between blebbistatin-treated and untreated groups are done using ANOVA.

This dependence on coherence is consistent with a recent computational study of cells moving on a fibrous surface (41).

Motivated by the critical role of cell shape in determining cell polarization, we wondered whether cell aspect ratio also dictates cell motility response to contact guidance. To address this question, we construct spatial maps of cell velocity for rounded ($a < 2$) and for elongated ($a > 3$) cells. As shown in Fig. 5 B and C, the velocity of elongated cells is highly correlated with the local fiber nematic order. Most elongated cells move in the tangential direction when they are close to the central particle ($\rho < 0.4$ mm), where ECM alignment is strong. Far away from the center ($\rho > 0.8$ mm), the direction of the velocity is nearly isotropic ($\langle \cos(\delta\theta) \rangle = 2/\pi$). In contrast, rounded cells largely ignore ECM contact guidance and do not demonstrate significant bias in their 3D migration direction. These results indicate that cell aspect ratio controls the motility response of a cell to noisy contact guidance cues. Interestingly, we find that the level of ECM alignment does not affect the persistence of cell migration velocity (Fig. 5D). Cells with strong bias in migration direction are free to move back and forth; see also ref. 43. Therefore, contact guidance is indeed nematic, rather than acting as an effectively unidirectional cue for cell migration.

To address whether these results are consistent with our cellular Potts model, we extend it to include a motility module. In this module, we incorporate a cell polarity vector, introduced by including an additional term in the Hamiltonian (see *SI Appendix, section S2*). The polarity of the cell can then change

with a probability that depends on the morphology of the cell. Simulations using this extended model are carried out as before, and we determine the cell's migration persistence, described by the autocorrelation function of the cell velocity, for different values of the coherence. Consistent with the experiments, the simulations show that this directional persistence is independent of the network coherence (Fig. 5D, *Inset*).

We have seen that ECM coherence regulates cell aspect ratio, with important consequences for motility guidance. We next examine the structural features of actin cytoskeleton of cells in the three identified subgroups. We find that elongated cells ($a > 3$) generally show F-actin filaments that grow parallel to the direction of the cell long axis. These cells show sharp finger-like membrane protrusions that are characteristic of filopodia and lamellipodia. Rounded cells ($a < 2$), on the other hand, have no clear F-actin fibers and typically exhibit bleb-like protrusions. Finally, cells in the intermediate morphology may show both blebbing and finger-like protrusions (Fig. 6A). Following literature conventions (44), we label cells with aspect ratio $a > 3$ as being in the mesenchymal mode (M), and cells with aspect ratio $a < 2$ in the amoeboid mode (A), while cells with

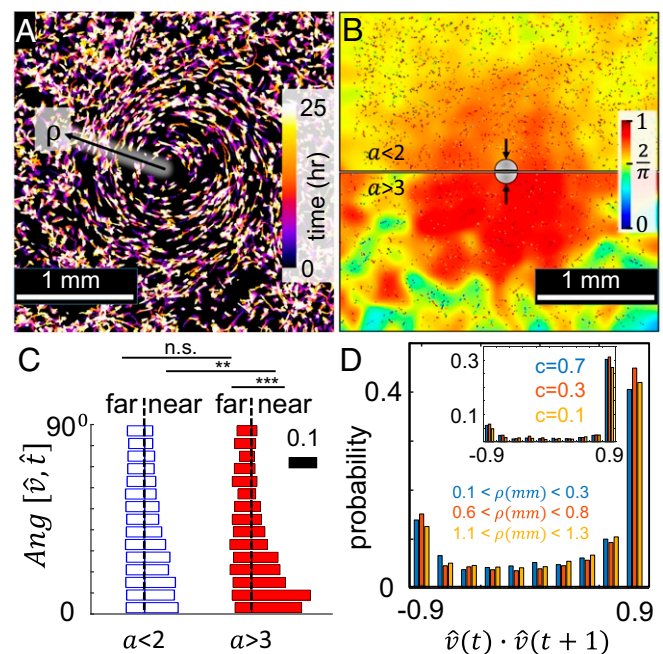


Fig. 5. Cell motility response to noisy 3D contact guidance cues. (A) A continuous recording (four frames per hour) of a typical experiment is projected using a color index linearly scaled with time. The projection reveals the trajectories of individual cells. (B) A spatial map of $\hat{v} \cdot \hat{t}$, where \hat{v} is the direction of instantaneous cell velocity (estimated by measuring cell displacement over 1 h), and \hat{t} is the tangential direction (also the direction of overall ECM fiber alignment); $\hat{v} \cdot \hat{t} = 1$ if a cell moves in the tangential direction; $\langle \hat{v} \cdot \hat{t} \rangle = \frac{2}{\pi}$ if cell velocity is random. (Upper) Cells with aspect ratios $a < 2$. (Lower) Cells with aspect ratios $a > 3$. The heat map is generated by spatially averaging individual cell data with a Gaussian kernel. The width of the Gaussian kernel is 100 μm , approximately the cell-to-cell distance. Arrows point to the location of central particle. (C) Probability distribution of the angle between cell velocity \hat{v} and tangential direction \hat{t} for rounded ($a < 2$) and elongated ($a > 3$) cells, both close to the center (near, $\rho < 0.4$ mm) and far from the center (far, $\rho > 0.8$ mm). n.s., not significant. $**P < 0.01$; $***P < 0.001$ with Kolmogorov-Smirnov test. (D) Directional persistence of cell motility as characterized by the probability distribution of inner products $\hat{v}(t) \cdot \hat{v}(t + 1)$. Here $\hat{v}(t)$ and $\hat{v}(t + 1)$ are the velocity directions of a cell at two consecutive hours. (*Inset*) Directional persistence of cell motility calculated with simulated cell trajectories (see *SI Appendix, section S2* for details). For each condition, more than 10,000 velocity instances are used to calculate the histogram.

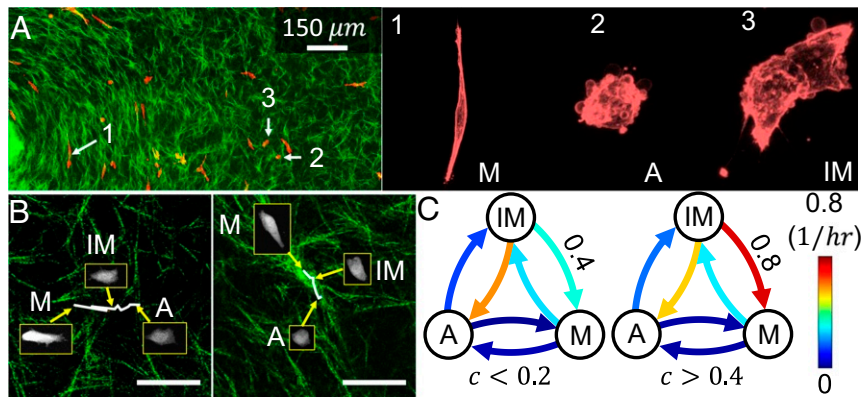


Fig. 6. Contact guidance cues modulate mode switching dynamics of 3D migrating cells. (A) Immunofluorescent imaging of MDA-MB-231 cells in an engineered collagen matrix. Red, actin cytoskeleton; green, collagen fibers. (Insets) Zoom-in views show that (location 1) an elongated cell exhibits fibrous actin cytoskeleton and sharp membrane protrusions, which are characteristic of an M mode of migration; (location 2) a rounded cell exhibits cortical actin and blebbing, which are characteristic of the A mode of migration; and (location 3) a cell in the IM mode exhibits both blebbing and sharp finger-shaped protrusion. (B) Two sample cell trajectories (white lines) plotted over the corresponding collagen matrices (green). Insets show that both cells exhibit mode transitions (M→IM→A for the cell in Left, A→IM→M for the cell in Right) when navigating the ECM. (Scale bars: 50 μm .) (C) Transition matrix (probability per hour) of cells among different modes for weakly aligned (Left; $c < 0.2$) and highly aligned ECM (Right; $c > 0.4$). The result is obtained by tracking a combined total of more than 1,000 h of single-cell trajectories.

aspect ratio $2 < a < 3$ are classified to be in an intermediate mode (IM).

To determine whether cells are able to switch between the different modes, we follow the morphodynamics of 3D migrating MDA-MB-231 cells as they navigate in the engineered collagen ECM. Fig. 6B shows two examples of trajectories of cells (white lines) and their dynamic morphologies. Fig. 6B, Left shows a cell in a low-coherence ECM ($c = 0.15$) that switches from a mesenchymal mode to an intermediate mode and, finally, to an amoeboid mode. Fig. 6B, Right shows a cell in a high-coherence ECM ($c = 0.5$) that switches from amoeboid to mesenchymal, through the intermediate mode.

By registering the transition events for single cells between A, M, and IM modes, we can construct the transition matrix of cellular states in both weakly aligned ECM ($c < 0.2$) and highly aligned ECM ($c > 0.4$). As shown in Fig. 6C, for both coherence values, the shape dynamics is highly stochastic, characterized by transitions between all modes. These transition rates are roughly constant for the two coherence values (see *SI Appendix, Table S1* for the transition matrix) except for the transition path IM→M, which increases twofold from 0.4 events per h to 0.8 events per h as the ECM coherence increases. In our data, this particular transition is responsible for the enrichment of elongated cells at stronger contact guidance cues.

Discussion

Noisy contact guidance by native tissue structures is a critical aspect of the physical microenvironment of cells (45). In this study, we experimentally mimic noisy 3D contact guidance with a simple magnetofluidics technique. Rather than controlling the ECM fiber alignment using external stress (19), our approach produces a flow-aligned gel, with spatially varying strength of this guidance cue. This allows us to focus on the effect of ECM geometry alone, and avoids any preloaded mechanical stress in the matrix. In addition, we explicitly consider the instantaneous local ECM structure in the immediate vicinity of each individual cell. Thus, compared to other coarse-grained studies, our analysis takes into account the intrinsic heterogeneity of the ECM. This local analysis is critical, since the microstructure of the ECM may vary significantly over distances comparable to the cell size (33). Even in regions with strong ECM alignment, we observe an approximately 15% fluctuation of measured coherence (Fig. 1). Therefore, correlating the polarization and motility of a cell with

its local ECM geometry accounts for the actual contact guidance cues presented to that cell.

Similar to previous reports (17, 19), we find that, when averaging over a large population of cells, stronger fiber alignment leads to more directed cell polarization and migration. As shown in Fig. 2C, cells with significant polarization (i.e., large aspect ratios) do respond better to more aligned ECM. However, we also show that an additional factor arises due to a coherence-dependent shift of the distribution of cell morphologies (Fig. 2D). Thus, we discover an intricate connection between the morphology of a cell and its response to contact guidance: Stronger contact guidance cues, corresponding to high-coherence ECMs, lead to more cells becoming elongated with large aspect ratios. These cells align to the principal ECM direction, and they do so increasingly well at higher coherence. On the other hand, even at high coherence, there remains a subgroup of cells with rounded shape, which does not at all follow contact guidance cues. Therefore, ECM alignment promotes changes in cell morphology, and this morphology change leads to cell alignment. Together, these two processes lead to the cellular response to contact guidance.

We have further shown that reallocation between the morphological subgroups is mediated by stochastic transitions between cellular states at the single-cell level. In particular, the transition rate from the intermediate state to the elongated (mesenchymal) state increases twofold as the ECM coherence increases, from less than 0.2 to greater than 0.4. This suggests that stabilization of nonblebbing protrusions may be a critical step for cells to integrate conflicting geometric cues in a noisy microenvironment (42).

Our experiments, theoretical calculations, and computer simulations all point to the special role of the aspect ratio in predicting the response of cells to 3D contact guidance. Biologically, the aspect ratio is a good classifier of mesenchymal versus amoeboidal phenotypes. These two phenotypes have been shown to demonstrate distinct cytoskeleton organization (Fig. 6A), protrusion dynamics, and migration characteristics (44, 46, 47). Previous reports show that cell contractility, which is regulated by Rho signaling, controls the sensitivity of cancer cells to contact guidance cues (19). Our results show that, for a given phenotype (mesenchymal or amoeboidal), the response to contact guidance is relatively independent of both actomyosin contractility and cell-ECM adhesion (Figs. 3E and 4). Taking together, this

suggests that Rho signaling regulates cancer cell response to contact guidance primarily by modulating the mesenchymal–amoeboid transition (48).

Physically, the cell's aspect ratio reflects the interplay between cell–ECM adhesion and cell contractility. Using both analytic and simulation models, we show that these two physical features control the mechanical balance of the cell–ECM system. The agreement between our models and experiments further testifies to the mechanical nature of cellular response to contact guidance. In addition, the velocity of an elongated cell is biased toward the direction of ECM fibers. The effect is stronger for higher ECM coherence and larger cell aspect ratio (Fig. 5 *B* and *C*). However, contact guidance does not increase the persistence of 3D cell migration (Fig. 5*D*). These characteristics of cell motility confirm that contact guidance is a nematic, rather than a unidirectional, physical cue for cells (43).

We have used a 2D model to help make sense of the data even though the experiments are taking place inside a full 3D ECM environment. Our experience is that the basic physics involved in these contact guidance experiments, namely, the bias in cell morphology due to adhesion to the fibers, does not depend, in any qualitative manner, on the dimensionality. This has already been shown to be true for other aspects of cell–ECM interactions (33, 49). Of course, if the density of collagen and its degree of cross-linking were dramatically increased, cells would face the extra challenge of fitting into the network pore space; this would be especially critical for their ability to translocate. In such a low-porosity matrix, one would have to resort to a much more complex modeling framework (50–52). We have also compared the results of our model with an alternative approach adapted from ref. 41. The results (*SI Appendix*, section S2 and Fig. S5) give us additional confidence that the basic physics of contact guidance can be correctly gleaned by simple models that focus on the critical role of cell adhesion and resultant cell morphology.

While the ECM guides cell polarization and migration, cells also can mechanically and chemically remodel the ECM. In our study, we have minimized the role of this remodeling by lowering the cell density and therefore have considered the ECM to be a static background. This is justified, as the principal direction and coherence of the ECM are not significantly changed by the presence of a nearby cell (*Movie S1*). This finding is in contrast to other studies that employ higher cell density. For example,

our recent work shows that, at high cell density, such as would be the case for a tumor organoid, contact guidance cues can be significantly and collectively remodeled by cells (20). An interesting future question is thus whether cell collectives sense contact guidance better than single cells, as they do for chemotaxis (53) and durotaxis (54).

Contact guidance from collagen fibers has direct clinical implications for cancer progression. Our study suggests that the underlying mechanism of fiber-directed cancer metastasis might rely on mechanically controlled cell phenotype selection. On the one hand, this highlights the importance of characterizing the physical microenvironment in cancer patients, which may be combined with cellular phenotype screening for precision diagnosis and prognosis. On the other hand, our results point to a comprehensive scheme where cellular behaviors can be programmed by aspects of their physical environment such as stiffness, geometry, and dimension. Future studies could address how physical, genetic, and biochemical means may be used to manipulate cell migration and morphology.

Materials and Methods

GFP-labeled MDA-MB-231 cells are purchased from GenTarget Inc., and are handled following the vendor's recommendations. High concentration rat tail type I collagen solutions are purchased from Corning Inc., and the collagen gels are prepared following standard protocol. Cells and collagen fibers are imaged using a Leica SPE confocal microscope with fluorescent and reflection channels simultaneously. A streamlined procedure using ImageJ, Matlab, and Python scripts was developed to analyze raw images. See *SI Appendix* for details of cell culture, microscopy, and image analysis. The statistical analysis and computer simulations are performed with Matlab (MathWorks®). See *SI Appendix* for details of simulation algorithms.

Data Availability. The images in the figures as well as additional microscopy images of the experiments are available at <https://figshare.com/account/home/projects/96863>. The cellular Potts model simulation codes are available at <https://github.com/caoys/cell-contact-cues.git>.

ACKNOWLEDGMENTS. We thank Drs. Joe W. Gray and Jing Yang for helpful discussions. This work is supported by Department of Defense Award W81XWH-20-1-0444 Program BC190068. J.K. is supported by NSF Grant PHY-1844627. H.L. is supported by the NSF Center for Theoretical Biological Physics (NSF Grant PHY-2019745) and also NSF Grant PHY-1935762. C.E. and B.S. are supported by National Institute of General Medical Sciences Grant R35GM138179.

1. J. Sutherland, M. Denyer, S. Britland, Contact guidance in human dermal fibroblasts is modulated by population pressure. *J. Anat.* **206**, 581–587 (2005).
2. K. Wolf *et al.*, Amoeboid shape change and contact guidance: T-lymphocyte crawling through fibrillar collagen is independent of matrix remodeling by MMPs and other proteases. *Blood* **102**, 3262–3269 (2003).
3. P. Friedl, S. Alexander, Cancer invasion and the microenvironment: Plasticity and reciprocity. *Cell* **147**, 992–1009 (2011).
4. W. P. Daley, K. M. Yamada, ECM-modulated cellular dynamics as a driving force for tissue morphogenesis. *Curr. Opin. Genet. Dev.* **23**, 408–414 (2013).
5. L. Lara Rodriguez, I. C. Schneider, Directed cell migration in multi-cue environments. *Int. Biol.* **5**, 1306–1323 (2013).
6. P. Roca-Cusachs, R. Sunyer, X. Trepat, Mechanical guidance of cell migration: Lessons from chemotaxis. *Curr. Opin. Cell Biol.* **25**, 543–549 (2013).
7. G. Balázs, A. Van Oudenaarden, J. J. Collins, Cellular decision making and biological noise: From microbes to mammals. *Cell* **144**, 910–925 (2011).
8. P. Friedl, E. B. Bröcker, The biology of cell locomotion within three-dimensional extracellular matrix. *Cell. Mol. Life Sci.* **57**, 41–64 (2000).
9. L. S. Tsimring, Noise in biology. *Rep. Prog. Phys.* **77**, 026601 (2014).
10. G. Potter, T. A. Byrd, A. J. Mugler, B. Sun, Dynamic sampling and information encoding in biochemical networks. *Biophys. J.* **112**, 795–804 (2017).
11. O. Symmons, A. Raj, What's luck got to do with it: Single cells, multiple fates, and biological nondeterminism. *Mol. Cell* **62**, 788–802 (2016).
12. A. D. Doyle, N. Carvajal, A. Jin, K. Matsumoto, K. M. Yamada, Local 3D matrix microenvironment regulates cell migration through spatiotemporal dynamics of contractility-dependent adhesions. *Nat. Commun.* **6**, 8720 (2015).
13. E. D. Tabdanov *et al.*, Bimodal sensing of guidance cues in mechanically distinct microenvironments. *Nat. Commun.* **9**, 4891 (2018).
14. G. A. Dunn, T. Ebendal, Contact guidance on oriented collagen gels. *Exp. Cell Res.* **111**, 475–479 (1978).
15. A. I. Teixeira, G. A. Abrams, P. J. Bertics, C. J. Murphy, P. F. Nealey, Epithelial contact guidance on well-defined micro- and nanostructured substrates. *J. Cell Sci.* **116**, 1881–1892 (2003).
16. V. C. Muderá *et al.*, Molecular responses of human dermal fibroblasts to dual cues: Contact guidance and mechanical load. *Cytoskeleton* **45**, 1–9 (2000).
17. M. K. Driscoll, X. Sun, C. Guven, J. T. Fourkas, W. Losert, Cellular contact guidance through dynamic sensing of nanotopography. *ACS Nano* **8**, 3546–3555 (2014).
18. D. A. Kulawiak, B. A. Camley, W. J. Rappel, Modeling contact inhibition of locomotion of colliding cells migrating on micropatterned substrates. *PLoS Comput. Biol.* **12**, e1005239 (2016).
19. P. P. Provenzano, D. R. Inman, K. W. Eliceiri, S. M. Trier, P. J. Keely, Contact guidance mediated three-dimensional cell migration is regulated by Rho/ROCK-dependent matrix reorganization. *Biophys. J.* **95**, 5374–5384 (2008).
20. J. Kim *et al.*, Geometric dependence of 3D collective cancer invasion. *Biophys. J.* **118**, 1177–1182 (2020).
21. M. W. Conklin *et al.*, Aligned collagen is a prognostic signature for survival in human breast carcinoma. *Am. J. Pathol.* **178**, 1221–1232 (2011).
22. P. Friedl, E. Sahai, S. Weiss, K. M. Yamada, New dimensions in cell migration. *Nat. Rev. Mol. Cell Biol.* **13**, 743–747 (2012).
23. K. M. Yamada, M. Sixt, Mechanisms of 3D cell migration. *Nat. Rev. Mol. Cell Biol.* **20**, 738–752 (2019).
24. E. Cukierman, R. Pankov, D. R. Stevens, K. M. Yamada, Taking cell-matrix adhesions to the third dimension. *Science* **294**, 1708–1712 (2001).
25. B. M. Baker, C. S. Chen, Deconstructing the third dimension—how 3D culture microenvironments alter cellular cues. *J. Cell Sci.* **125**, 3015–3024 (2012).
26. M. Krause, K. Wolf, Cancer cell migration in 3D tissue: Negotiating space by proteolysis and nuclear deformability. *Cell Adhes. Migrat.* **9**, 357–366 (2015).
27. C. P. Broedersz, F. C. MacKintosh, Modeling semiflexible polymer networks. *Rev. Mod. Phys.* **86**, 995 (2014).

28. C. Guo, L. J. Kaufman, Flow and magnetic field induced collagen alignment. *Biomaterials* **28**, 1105–1114 (2007).
29. J. P. R. O. Orgel, T. C. Irving, A. Miller, T. J. Wess, Microfibrillar structure of type I collagen in situ. *Proc. Natl. Acad. Sci. U.S.A.* **103**, 9001–9005 (2006).
30. G. Duclos, C. Erlenkämper, J. Joanny, P. Silberzan, Topological defects in confined populations of spindle-shaped cells. *Nat. Phys.* **13**, 58–62 (2017).
31. Z. Püspöki, M. Storath, D. Sage, M. Unser, "Transforms and operators for directional bioimage analysis: A survey" in *Focus on Bio-Image Informatics, Advances in Anatomy, Embryology and Cell Biology*, W. De Vos, S. Munck, J. P. Timmermans, Eds. (Springer International, 2016), vol. 219, pp. 69–93.
32. C. A. R. Jones, L. Liang, D. Lin, Y. Jiao, B. Sun, The spatial-temporal characteristics of type I collagen-based extracellular matrix. *Soft Matter* **10**, 8855–8863 (2014).
33. C. A. R. Jones et al., Micromechanics of cellularized biopolymer networks. *Proc. Natl. Acad. Sci. U.S.A.* **37**, E5117 (2015).
34. F. Beroz et al., Physical limits to biomechanical sensing in disordered fibre networks. *Nat. Commun.* **8**, 16096 (2017).
35. A. A. Alobaidi, B. Sun, Probing three-dimensional collective cancer invasion with DIGME. *Canc. Conver.* **1**, 1 (2017).
36. F. Graner, J. A. Glazier, Simulation of biological cell sorting using a two-dimensional extended potts model. *Phys. Rev. Lett.* **69**, 2013–2016 (1992).
37. W. J. Rappel, A. Nicol, A. Sarkissian, H. Levine, W. F. Loomis, Self-organized vortex state in two-dimensional dictyostelium dynamics. *Phys. Rev. Lett.* **83**, 1247 (1999).
38. A. J. Kabla, Collective cell migration: Leadership, invasion and segregation. *J. R. Soc. Interface* **9**, 3268–3278 (2012).
39. A. Szabó, R. M. Merks, Cellular potts modeling of tumor growth, tumor invasion, and tumor evolution. *Front. Oncol.* **3**, 87 (2013).
40. E. G. Rens, L. Edelstein-Keshet, From energy to cellular forces in the cellular potts model: An algorithmic approach. *PLoS Comput. Biol.* **15**, e1007459 (2019).
41. J. Feng, H. Levine, X. Mao, L. M. Sander, Cell motility, contact guidance, and durotaxis. *Soft Matter* **15**, 4856–4864 (2019).
42. G. R. Ramirez-San Juan, P. W. Oakes, M. L. Gardel, Contact guidance requires spatial control of leading-edge protrusion. *Mol. Biol. Cell* **28**, 1043–1053 (2017).
43. S. I. Fraley, Y. Feng, A. Giri, G. D. Longmore, D. Wirtz, Dimensional and temporal controls of three-dimensional cell migration by zyxin and binding partners. *Nat. Commun.* **3**, 1–13 (2012).
44. C. D. Paul, P. Mistrionis, K. Konstantopoulos, Cancer cell motility: Lessons from migration in confined spaces. *Nat. Rev. Canc.* **17**, 131 (2017).
45. C. M. Nelson, M. J. Bissell, Of extracellular matrix, scaffolds, and signaling: Tissue architecture regulates development, homeostasis, and cancer. *Annu. Rev. Cell Dev. Biol.* **22**, 287–309 (2006).
46. R. J. Petrie, K. M. Yamada, At the leading edge of three-dimensional cell migration. *J. Cell Sci.* **125**, 5917–5926 (2012).
47. K. Wolf et al., Compensation mechanism in tumor cell migration. *J. Cell Biol.* **160**, 267–277 (2003).
48. V. Sanz-Moreno et al., Rac activation and inactivation control plasticity of tumor cell movement. *Cell* **135**, 510–523 (2008).
49. J. Kim et al., Stress-induced plasticity of dynamic collagen networks. *Nat. Commun.* **8**, 1–7 (2017).
50. M. C. Kim, Y. R. Silberberg, R. Abeyaratne, R. D. Kamm, H. H. Asada, Computational modeling of three-dimensional ecm-rigidity sensing to guide directed cell migration. *Proc. Natl. Acad. Sci. U.S.A.* **115**, E390–E399 (2018).
51. H. Ahmadzadeh et al., Modeling the two-way feedback between contractility and matrix realignment reveals a nonlinear mode of cancer cell invasion. *Proc. Natl. Acad. Sci.* **114**, E1617–E1626 (2017).
52. X. Chen, V. te Boekhorst, E. McEvoy, P. Friedl, V. B. Shenoy, An active chemo-mechanical model to predict adhesion and microenvironmental regulation of 3D cell shapes. *bioRxiv [Preprint]* (2021). <https://doi.org/10.1101/2020.01.07.897405> (Accessed 20 April 2021).
53. D. Ellison et al., Cell-cell communication enhances the capacity of cell ensembles to sense shallow gradients during morphogenesis. *Proc. Natl. Acad. Sci. U.S.A.* **113**, E679–E688 (2016).
54. R. Sunyer et al., Collective cell durotaxis emerges from long-range intercellular force transmission. *Science* **353**, 1157–1161 (2016).